

PAPER • OPEN ACCESS

Design and feasibility of a flexible, on-body, high impedance coil receive array for a 1.5 T MR-linac

To cite this article: Stefan E Zijlema *et al* 2019 *Phys. Med. Biol.* **64** 185004

View the [article online](#) for updates and enhancements.

RUBY Modular QA Phantom

Performs end-to-end tests of the
entire stereotactic treatment chain

 **PTW**
THE
DOSIMETRY
COMPANY



OPEN ACCESS



PAPER

Design and feasibility of a flexible, on-body, high impedance coil receive array for a 1.5 T MR-linac

RECEIVED
21 March 2019REVISED
25 July 2019ACCEPTED FOR PUBLICATION
1 August 2019PUBLISHED
11 September 2019

Original content from this work may be used under the terms of the [Creative Commons Attribution 3.0 licence](https://creativecommons.org/licenses/by/3.0/).

Any further distribution of this work must maintain attribution to the author(s) and the title of the work, journal citation and DOI.

Stefan E Zijlema^{1,2}, Rob H N Tijssen¹, Victor N Malkov¹, Luca van Dijk¹, Sara L Hackett¹, Jan G M Kok¹, Jan J W Lagendijk¹ and Cornelis A T van den Berg^{1,2}¹ Department of Radiotherapy, Universitair Medical Center Utrecht, Utrecht, The Netherlands² Computational Imaging Group for MR Diagnostics & Therapy, Center for Image Sciences, University Medical Center Utrecht, The NetherlandsE-mail: s.e.zijlema@umcutrecht.nl**Keywords:** MR-linac, radiolucent, low attenuation, high impedance coil, receive array, MRI-guided radiotherapy**Abstract**

The lack of radiation-attenuating tuning capacitors in high impedance coils (HICs) make HICs an interesting building block of receive arrays for MRI-guided radiotherapy (MRIgRT). Additionally, their flexibility and limited channel coupling allow for low-density support materials, which are likely to be more radiation transparent (radiolucent). In this work, we introduce the use of HICs in receive arrays for MRIgRT treatments. We discuss the design and show the dosimetric feasibility of a HIC receive array that has a high channel count and aims to improve the imaging performance of the 1.5 T MR-linac. Our on-body design comprises an anterior and posterior element, which each feature a 2×8 channel layout (32 channels total). The anterior element is flexible, while the posterior element is rigid to support the patient. Mockups consisting of support materials and conductors were built, irradiated, and optimized to minimize impact on the surface dose (7% of the dose maximum) and dose at depth ($\leq 0.8\%$ under a single conductor and $\leq 1.4\%$ under a conductor crossing). Anatomical motion and the use of multiple beam angles will ensure that these slight dose changes at depth are clinically insignificant. Subsequently, several functional, single-channel HIC imaging prototypes and a 5-channel array were built to assess the performance in terms of signal-to-noise ratio (SNR). The performance was compared to the clinical MR-linac array and showed that the 5-channel imaging prototype outperformed the clinical array in terms of SNR and channel coupling. Imaging performance was not affected by the radiation beam. In conclusion, the use of HICs allowed for the design of our flexible, on-body receive array for MRIgRT. The design was shown to be dosimetrically feasible and improved the SNR. Future research with a full array will need to show the gain in parallel imaging performance and thus acceleration.

1. Introduction

Several hybrid MRI-radiotherapy systems have been developed in an effort to improve radiation therapy treatments, i.e. to ensure tumor coverage and minimize toxicity, using MRI to monitor positions of mobile tumors and organs at risk (Fallone 2014, Keall *et al* 2014, Lagendijk *et al* 2014, Mutic and Dempsey 2014). However, MRI is known to be inherently slow. Long acquisition times lengthen preparatory (pre-beam) imaging and limit real-time anatomy monitoring to 2D planes or low-resolution 3D volumes. A receive array with a high channel count can overcome this limitation by enabling the use of high undersampling factors through its increased parallel imaging (PI) capabilities (Pruessmann *et al* 1999, Larkman *et al* 2001, Breuer *et al* 2005).

The 1.5 T Elekta MR-linac (Unity, Elekta AB, Stockholm, Sweden) is equipped with a clinical receive array that consists of two 4-channel elements, which are positioned centimeters away from the anatomy: the anterior element is elevated above the patient and the posterior element is positioned under the table (Hoogcarspel *et al* 2018). The limited channel count, combined with the 1×4 -channel arrangements and distant positioning, limits the SNR and PI performance in all planes.

A dense³, on-body receive array for the MR-linac could considerably improve the imaging performance, both during the preparatory pre-beam phase, as well as during irradiation. However, the design and on-body placement of such an array are not trivial, as the radiation beam passes through during treatments, which has two major dosimetric consequences. Firstly, the array may function as bolus and increase the patient's surface dose (Ghila *et al* 2016). The surface dose of patients is currently minimized by the elevated design of the clinical array. The elevation allows most secondary electrons that are generated in the coil materials, to be bent off by the magnetic field before they reach the patient's skin (Raaijmakers *et al* 2005). This so-called electron return effect (ERE) will not reduce the surface dose when dense coil materials are placed directly onto the patient, as the electrons have no space to curve back. A second dosimetric consequence of the receive array is that its electronics and support materials could cause local attenuation of the treatment beam (Hoogcarspel *et al* 2013). A large region in the center of the array is required that does not attenuate the beam, i.e. a radiolucent window. However, conventional, low impedance coils (LICs) use multiple capacitors that are distributed over the loop (Vaughan *et al* 1994), which would attenuate the treatment beam due to their dense structure. The current clinical array solves this issue by restricting the amount of capacitors per loop to two and placing these on the cranial and caudal sides outside the radiolucent window. However, when a second row would be added to maximize the number of channels, only one capacitor can be placed per coil, which, combined with the smaller loop sizes, will lead to severe channel coupling. Unlike LICs, the recently proposed high impedance coils (HICs) do not require capacitors in the loop (Zhang *et al* 2018). Instead, the distributed capacitance of the coaxial conductor is used for tuning. Zhang *et al* showed that HICs can be very flexible and exhibit limited coupling interactions with neighboring loops. A HIC receive array therefore requires less-critical overlap optimization than LICs to achieve the optimal imaging performance and consequently does not demand dense support materials to firmly secure the geometry. This will be beneficial for the array's radiolucency and thus makes HICs an attractive building block of a radiolucent receive array for MRI-guided radiotherapy (MRIgRT).

In this work, we introduce the use of HICs in receive arrays for MRI-guided radiotherapy treatments and discuss the design and feasibility of a dense HIC receive array for on-body placement to improve the imaging performance of the 1.5 T MR-linac. The anterior element is flexible in order to closely match the body contour of all patients. The posterior element is placed directly under the patient for optimal imaging sensitivity. The full array allows for the use of up to 32 channels. All aspects of the design are optimized to minimize the impact on the radiation therapy, e.g. the composition and thickness of the support materials and conductors. Ideally, its impact is kept as low as possible. This way, the array does not require inclusion in the treatment planning system (TPS) or tracking of the dynamic position over time, which greatly simplifies its use. Finally, functional, single-channel and 5-channel prototypes are built and the gain in SNR from our on-body approach is quantified with respect to the current clinical array, both with and without a radiation beam enabled.

2. Methods

2.1. Proposed design

Major changes are made to the coil design with respect to the clinical array (figure 1). Flexible HICs are used instead of LICs. The anterior element is no longer rigid and elevated, but is placed on the patient and can bend to fit any anatomy. The posterior element is placed on the table, directly under the patient. The single-row layout is replaced by a double-row layout, which will provide extra spatially varying coil sensitivities in the feet-head direction for enhanced PI capabilities. This will require cable outputs on two sides of the array (feet and head) and consequently both ends of the bore, as the data and power cables cannot run through the radiolucent window. Each channel can be connected with a coaxial cable to an in-house developed interface box on the table, which performs preamplification and digitization of the signal. From here, the data are transferred to the system via an optical fiber. The final anterior and posterior element will comprise 16 channels each, totaling 32 channels when both elements are used simultaneously (table 1).

Support materials of the array were chosen to have a low mass density, which is expected to lead to a low electron density and thus a low dosimetric impact. The HIC's flexibility allows for the removal of sturdy, dense layers that are required for LICs to fix their relative positioning that is essential for minimizing channel coupling. This will allow easier bending of the array and improves radiolucency. The support material thicknesses were also optimized. For optimal sensitivity in the body, the coil loops should be as close to the patient as possible. However, as discussed before, dense loop materials can increase the surface dose. Here, the use of low-density foam between the loops and the patient is investigated to reduce this so-called bolus effect (figure 2). The resulting distance is expected to allow the secondary electrons that are generated in the dense materials to be absorbed or bent off by the Lorentz force from the perpendicular magnetic field (Raaijmakers *et al* 2005).

³ A dense array is a coil engineering term that refers to an array with a large number of channels that densely cover a surface. It should not be confused with a high mass or electron density.

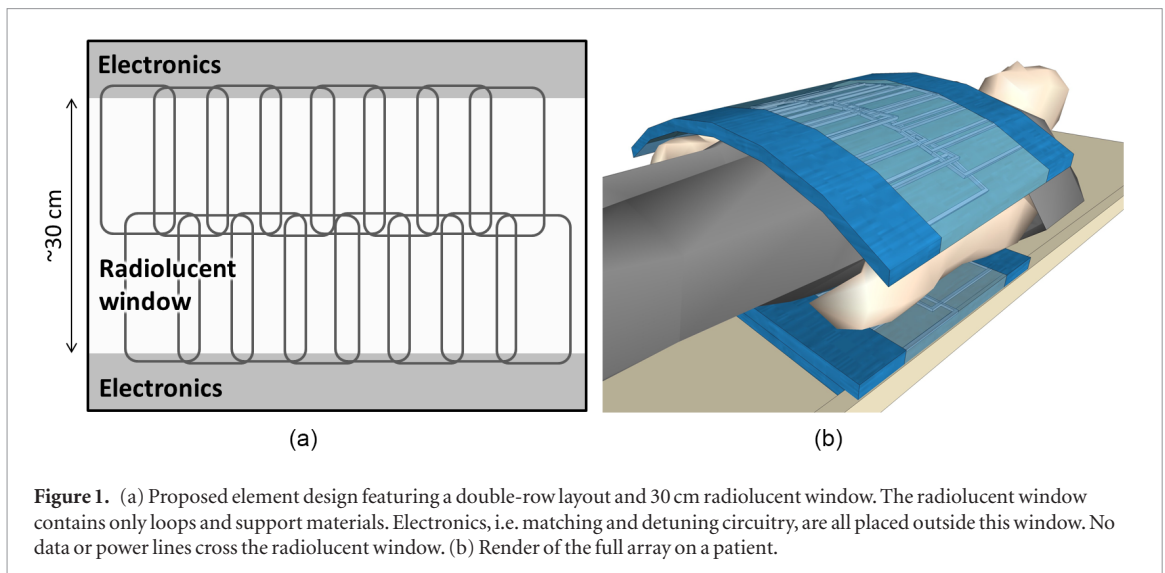
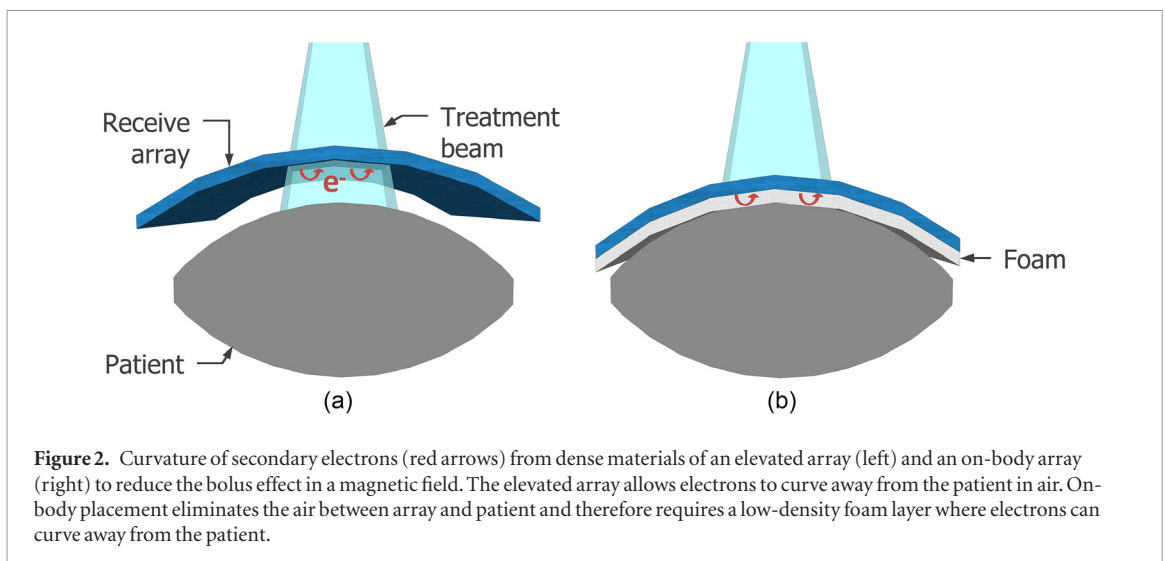


Table 1. Coil dimension comparison between the current clinical array of the 1.5 T MR-linac and the proposed design.

	Clinical array	Proposed design
Nr. channels (total)	8	32
Nr. channels per element	4	16
Nr. channels (RL)	4	8
Nr. channels (FH)	1	2
Single channel width (RL)	~128 mm	~90 mm
Single channel length (FH)	~440 mm	~190 mm



2.2. Dosimetry

Above hypotheses, as well as the attenuation of the conductors, are dosimetrically investigated by quantifying the design's bolus effect at the surface and dose reduction at larger depths. Monte Carlo simulations were performed to investigate beam angulation effects.

2.2.1. Bolus effect minimization

Several mockups were manufactured to investigate and minimize the bolus effect. First, three mockups of the anterior element (mockups_{ant}) were created with varying foam thicknesses (figure 3(a)/(b)). The low (electron) density foam serves as a spacer between the materials with high electron density (i.e. the conductors) and the patient's skin. Between the foam layers of the mockups, three candidate HIC coaxial cable types were placed with partially overlapping strands. AlphaWire (Elizabeth, NJ, USA) 9434 (ϕ 1.0 mm), AlphaWire 9432 (ϕ 1.1 mm), and

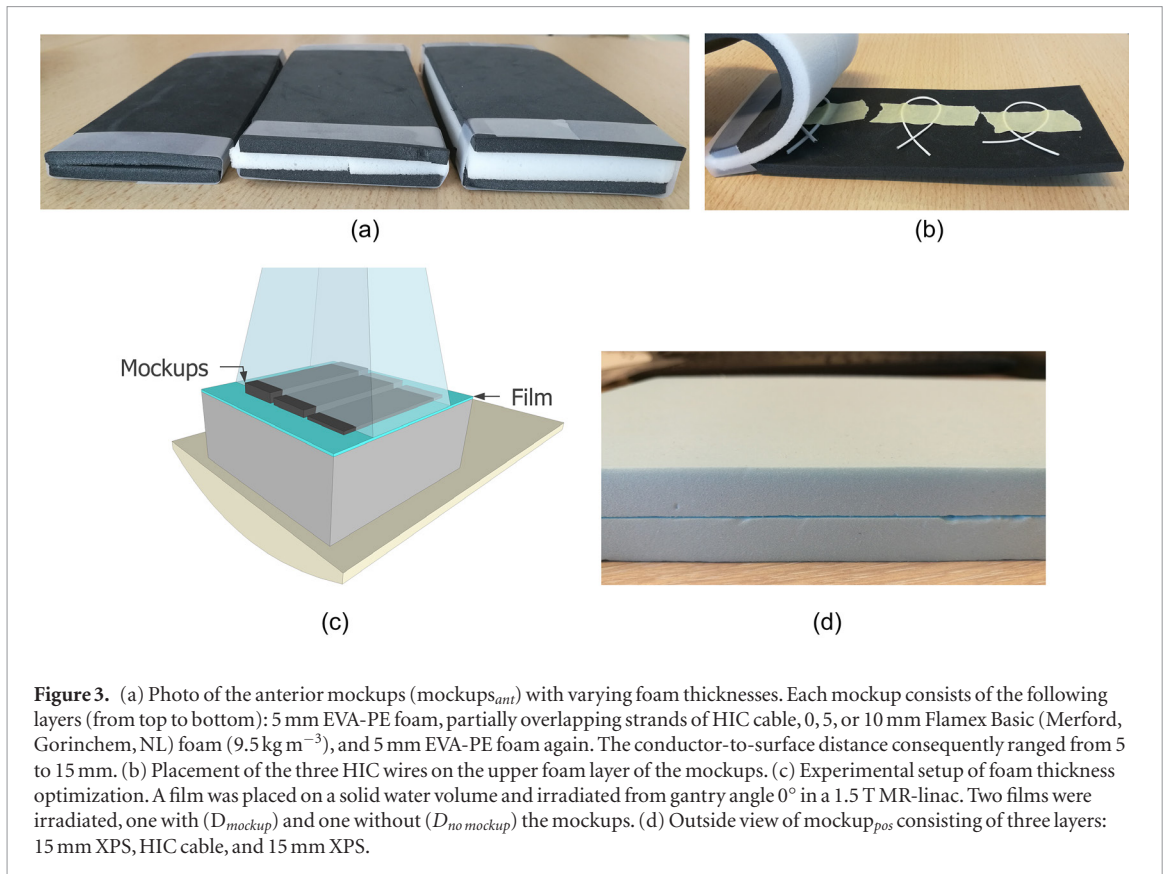


Figure 3. (a) Photo of the anterior mockups ($mockups_{ant}$) with varying foam thicknesses. Each mockup consists of the following layers (from top to bottom): 5 mm EVA-PE foam, partially overlapping strands of HIC cable, 0, 5, or 10 mm Flamex Basic (Merford, Gorinchem, NL) foam (9.5 kg m^{-3}), and 5 mm EVA-PE foam again. The conductor-to-surface distance consequently ranged from 5 to 15 mm. (b) Placement of the three HIC wires on the upper foam layer of the mockups. (c) Experimental setup of foam thickness optimization. A film was placed on a solid water volume and irradiated from gantry angle 0° in a 1.5 T MR-linac. Two films were irradiated, one with (D_{mockup}) and one without ($D_{no\ mockup}$) the mockups. (d) Outside view of $mockup_{pos}$ consisting of three layers: 15 mm XPS, HIC cable, and 15 mm XPS.

RG178 ($\phi 1.8 \text{ mm}$) cables were used, of which the latter was also used by Zhang *et al* (2018) for a flexible hand array. These will henceforth be referred to as $wire_{1,0}$, $wire_{1,1}$, and $wire_{1,8}$, respectively.

The $mockups_{ant}$ were irradiated on a 1.5 T MR-linac with a 7 MV, 400 MU, $57 \times 22 \text{ cm}^2$ field (figure 3(c)) and a source-surface distance (SSD) of 142 cm. A GAFChromic (Ashland, USA) EBT-3 film (lot: 07181601) was placed at the surface and the dose was measured without a mockup ($D_{no\ mockup}$) and with the mockups placed directly onto the film (D_{mockup}). Films were scanned with an Epson Expression 10000XL flatbed scanner. Films were aligned and converted to dose with an in-house, clinically used tool. The dose change ΔD was calculated with:

$$\Delta D = D_{mockup} - D_{no\ mockup}. \quad (1)$$

As a reference, the measurement was repeated with a gantry angle of 180° to see the bolus effect due to the treatment couch. The dose was corrected for the different beam characteristics.

2.2.2. Dosimetry at depth

Film dosimetry was found to be insufficiently accurate for a dosimetric comparison at depth, as inhomogeneities in the film were larger than the expected dose changes of a few percent or less. Instead, an electronic portal imaging device (EPID) was used to spatially quantify the dose changes with a high resolution ($0.25 \times 0.25 \text{ mm}^2$). The response of an aSi EPID panel has been shown to be linear with dose (Grein *et al* 2002), thus the relative dosimetric impact of the mockups can be quantified. The correspondence between EPID signal and dose is validated using ionization chamber measurements in appendix A.

All EPID imaging was performed on a conventional linac (Synergy, Elekta AB) without a magnetic field present so that the setup could be placed against the panel. Images were acquired with the XIS (PerkinElmer, Waltham, MA, USA) software package with an acquisition time of 433 ms per frame. A 100 MU $10 \times 10 \text{ cm}^2$ 6 MV beam was delivered at a gantry angle of 90° with a dose rate of 250 MU min^{-1} . A 100-frame average was saved that covered the full beam delivery. All automatic corrections were disabled. A five-minute waiting step was employed between acquisitions to avoid ghosting effects. Measurements assessed the radiolucency of an optimized $mockup_{ant}$ (figure 3(a)) and of a posterior $mockup_{pos}$ (figure 3(d)), of which the latter featured non-flexible foam layers, as the array has to support the patient.

First, two reference images are acquired without mockup or phantom present to normalize the EPID response: an open flood-field image (I_{flat}) and a dark-field image without irradiation (I_{dark}). Subsequently, 100 mm solid water was placed against the EPID panel (SSD = 150 cm). EPID measurements were performed with and without placement of a mockup against the phantom. Prior to each acquisition, a new dark image was acquired (I_{dark_dyn}). The raw images (I_{raw}) were then processed with (McDermott *et al* 2004):

$$I_{proc} = \frac{I_{raw} - I_{dark_dyn}}{I_{flat} - I_{dark}}. \quad (2)$$

The dose attenuation fraction due to the mockup (A_{EPID}) can then be found by simply calculating the relative change:

$$A_{EPID} = \frac{I_{proc, mockup} - I_{proc, no\ mockup}}{I_{proc, no\ mockup}}. \quad (3)$$

2.2.3. Monte Carlo simulations

Monte Carlo simulations were used to investigate the influence of angulated, non-perpendicular beams on the dose changes. Additionally, simulations were performed to translate the EPID measurements without a magnetic field to an expected dose change at 1.5 T. The correspondence between the EPID signal and the Monte Carlo simulations with and without a magnetic field is discussed in appendix B.

Engine and beam characteristics

The `egs_chamber` application (Wulff *et al* 2008) of the EGSnrc Monte Carlo package (Kawrakow and Rogers 2000) was used for all simulations. The magnetic field transport is included using the enhanced electric and magnetic field macros (Malkov and Rogers 2016). The electron and photon total energy cut-offs were set to 661 keV and 10 keV, respectively. The latest available Elekta-provided phase-space data for the 7 MV FFF Elekta Unity accelerator were used. These data define a $10 \times 10 \text{ cm}^2$ field at isocenter, located 143.5 cm away from the source and stores the particles in the phase space at 128.5 cm from the source. Both electrons and photons were provided in the phase-space and included in the simulation. For tilted beam simulations a photon spectrum is extracted from the phase-space and used instead.

Simulated setup

The receive array is modeled with the same composition as `mockupant` with a conductor-to-surface distance of 15 mm (figure 3(a)). The dimensions and material compositions from the manufacturer's datasheets were used. The conductors are simulated as two perpendicular, straight coaxial cables that cross in the center. For practical reasons, only the `wire1,1` prototype was simulated.

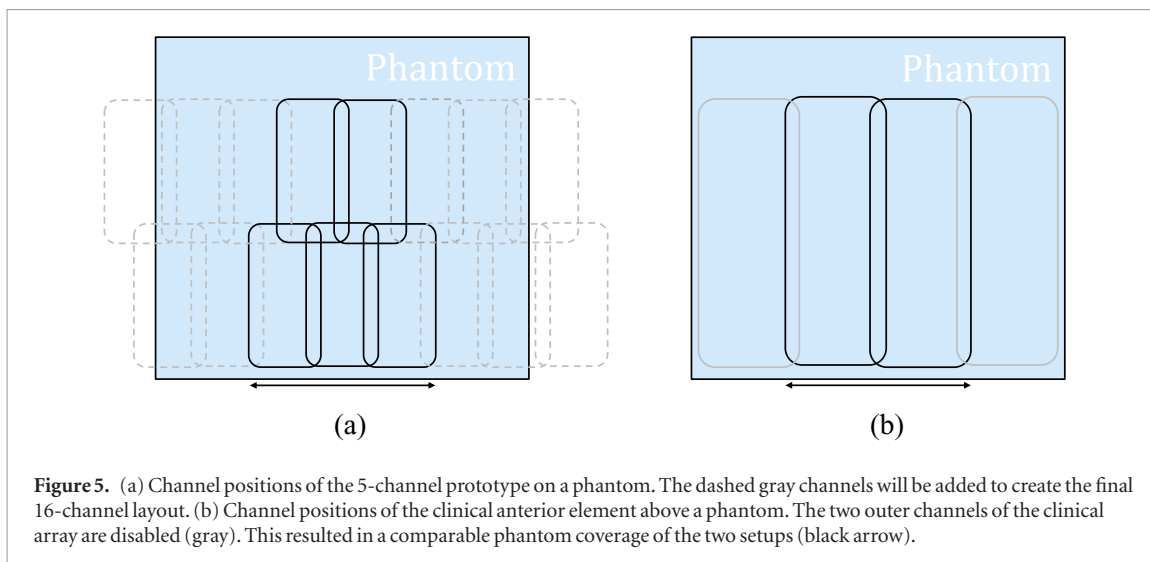
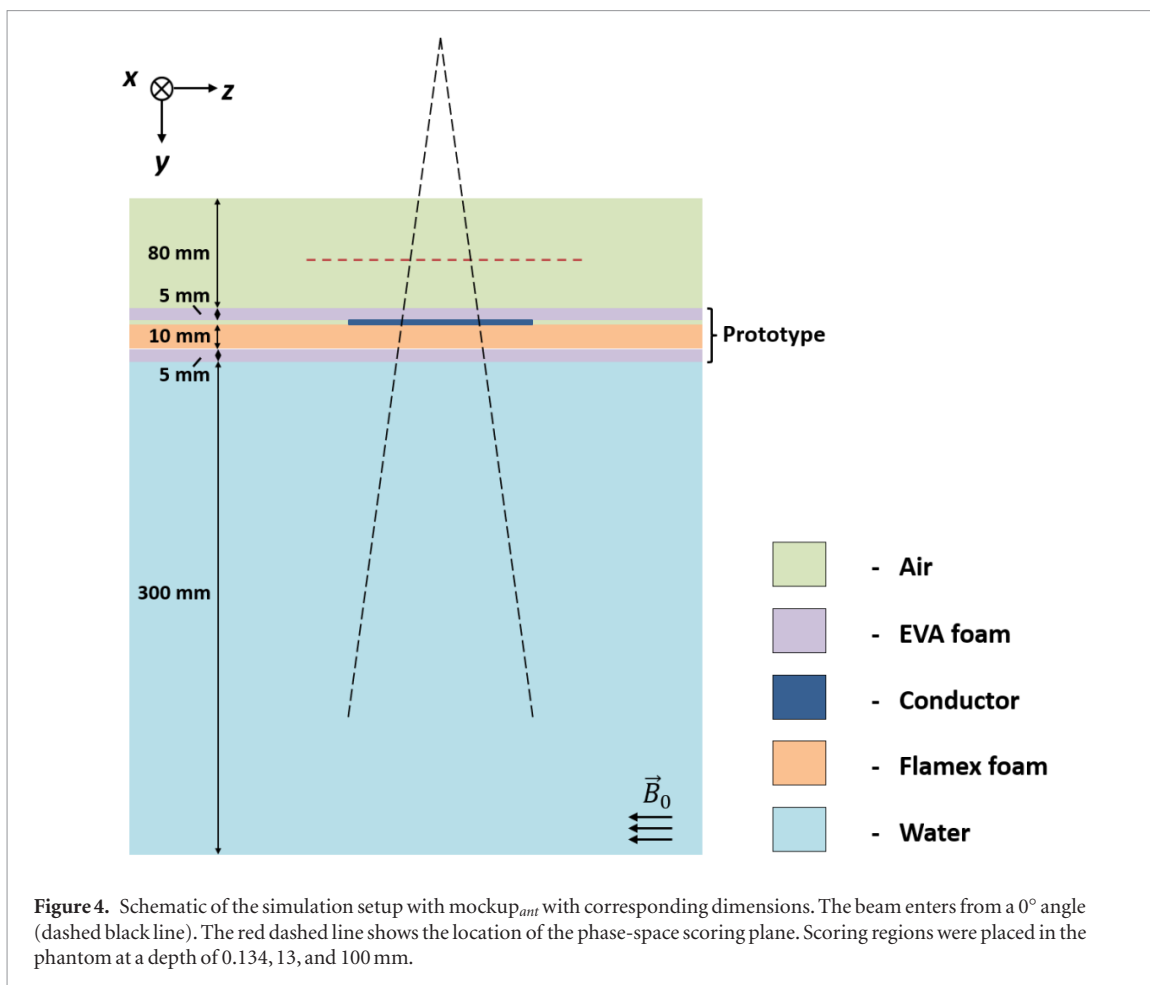
The simulated setup is shown in figure 4. A $30 \times 30 \times 30 \text{ cm}^3$ water phantom is positioned with an SSD of 133.5 cm. An 8 cm layer of air is positioned on top in the simulations without prototype. When the prototype is present, it replaces the air in the region closest to the phantom. Simulations with a 1.5 T magnetic field are run with beams incoming at a 0° , $\pm 30^\circ$ and $\pm 55^\circ$ rotation around the z -axis. The rotation will cause a higher path length through the conductor, which is expected to increase the attenuation. Higher angles than 55° are unlikely, as the array will fold around the patient and thus most beams will hit the array approximately perpendicularly. The field sizes were set to be $10 \times 10 \text{ cm}^2$ in the isocenter.

Scoring and analysis

As the (surface) dose will vary greatly within the first mm, $1 \times 1 \times 1 \text{ mm}^3$ voxels will give an inaccurate representation of the surface dose. Therefore, a thin single voxel of dimension $20 \times 20 \times 0.028 \text{ mm}^3$ is analyzed at a depth of 0.134 mm to reflect the sensitive region of an EBT-3 film that is placed on top of a phantom. This way, the simulations can be compared to the experimental findings. At depth, two scoring regions are set up as $101 \times 101 \times 1$ matrices with 1 mm^3 voxels. The regions are positioned at 13 mm (D_{max}) and 100 mm depth in the water phantom. All simulations were performed with and without the prototype on the phantom and the relative change was calculated (A_{sim}).

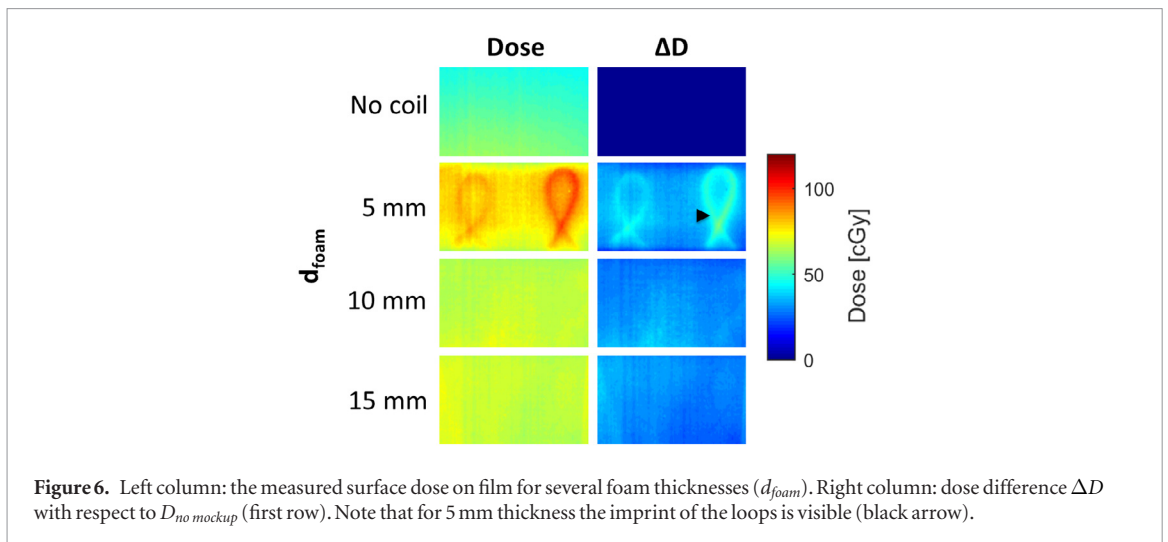
2.3. Imaging

The imaging performance of single-channel prototypes and a 5-channel prototype array were investigated in this work. High-impedance coils ($\sim 9 \times 19 \text{ cm}^2$) were constructed from coaxial `wire1,0`, `wire1,1`, and `wire1,8` and cable lengths were adjusted for resonance at 63.87 MHz (Zhang *et al* 2018). The loops were connected to matching and detuning circuitry, which in turn connected to an interfacing box with the preamplification and digitization hardware. Bending of the loops around a phantom during bench tests did not affect the matching significantly ($< 1 \text{ dB}$) and should therefore not affect the imaging performance. To assess the impact of channel coupling on the imaging performance, five `wire1,1` loops were combined into an array (figure 5(a)) and its performance was compared to the clinical anterior element with its two center channels enabled (figure 5(b)), such that the phantom coverage of the two arrays was approximately equal.



All imaging was performed on a 1.5 T Elekta Unity MR-linac using a pelvis-sized phantom (PVP- and agar-based, 2.6% NaCl) with dielectric properties that are representative of a human body. Prototypes were placed onto the phantom on a 15 mm foam spacer. The anterior element of the clinical array was elevated 3 cm above the phantom, i.e. in treatment position.

For the single-channel prototypes, 2D spoiled gradient echo acquisitions ($TR/TE = 30/4.0$ ms, flip angle = 20°, $FOV = 420 \times 240$ mm², voxel size = $3 \times 3 \times 10$ mm³) were performed. For the multi-channel arrays, transverse and sagittal 3D spoiled gradient echo acquisitions ($TR/TE = 30/4.0$ ms, flip angle = 40°, $FOV = 66 \times 40 \times 25$ cm³, voxel size = $3 \times 3 \times 10$ mm³) were performed. The raw k-space data were reconstructed using ReconFrame (Gyrotools, Zurich, CH). For the multi-channel acquisitions, sum-of-squares channel combination was performed.



The SNR was calculated (Kellman and McVeigh 2005) and used as a performance metric. Furthermore, channel coupling was quantified from the noise-only pre-scan by calculating the Pearson correlation coefficients.

Finally, the impact of the radiation beam on the SNR is investigated. Burke *et al* (2010) described radiation-induced signal spikes in k-space when a receive array is irradiated, which can lead to a reduction in SNR. The effect of radiation was assessed for the wire_{1,1} single-channel prototype and a single channel of the clinical anterior element. A 50-dynamic spoiled gradient echo (TR/TE = 7.3/2.3 ms) acquisition was performed with and without a $15 \times 15 \text{ cm}^2$ beam that crossed the loop. Under the assumption that the signal from the phantom is stationary, we can use the time-course SNR as a metric for the SNR (Sijbers *et al* 1998, Kellman and McVeigh 2005). Radiation-induced spikes in k-space will disrupt the stationary signal and consequently lower the time-course SNR. Using the dynamic imaging series, we can calculate the SNR with:

$$\text{SNR}(x, y) = \frac{S_{mean}(x, y)}{\sigma(x, y)}, \quad (4)$$

where $S_{mean}(x, y)$ and $\sigma(x, y)$ are the mean and standard deviation of the magnitude pixel intensity over time at location (x, y) , respectively.

3. Results

3.1. Dosimetry

3.1.1. Bolus effect minimization

The dose without a mockup ($D_{no\ mockup}$) equaled 15% with respect to the dose maximum (D_{max}) at 13 mm. As expected, placement of the mockups_{ant} increases the surface dose, but the addition of low-density foam layers is shown to decrease the bolus effect from the dense materials (figure 6). Here, d_{foam} represents the conductor-to-surface distance, as explained in figure 3. An increase from 5 mm to 10 or 15 mm decreased the surface dose from 29% (directly under the conductor of $D_{mockup_{ant},5\ mm}$) to 22% ($D_{mockup_{ant},10\ mm}$ and $D_{mockup_{ant},15\ mm}$) of D_{max} . In comparison, a posterior beam through the treatment couch more than doubled the surface dose to 40% of D_{max} .

3.1.2. Dosimetry at depth

Table 2 shows the dose attenuation fractions, obtained by EPID measurements, due to the prototypes and their corresponding support materials at 10 cm depth. The weight-bearing support materials of posterior mockup_{pos} (support_{pos}) attenuate more than the flexible foam layers of anterior mockup_{ant} (support_{ant}). Mockup_{ant}, which contains wire_{1,1} conductors, induces local dose reductions of $\leq 1.4\%$.

3.1.3. Monte Carlo simulations

The $28 \mu\text{m}$ surface dose simulations at 1.5 T showed a $46.7\% \pm 0.2\%$ increase of the surface dose with a 0° beam angle, which equals 7% of D_{max} . Similar simulations from a -55° and $+55^\circ$ angle resulted in a $39.3\% \pm 0.2\%$ increase (6% of D_{max}) and a $3.5\% \pm 0.1\%$ decrease (0.5% of D_{max}) of the surface dose, respectively.

Table 3 shows the prototype-induced dose attenuation fractions at several beam angles. The attenuation of the support materials stays $\leq 0.3\%$. The cable results in local decreases of up to 1.5% for conductor crossings at 0° . Larger beam angles result in slightly larger dose changes: up to 2.1%. Values at 13 and 100 mm depth are approximately equal.

Table 2. Dose attenuation fractions obtained by EPID measurements (A_{EPID}) due to the prototype materials at a depth of 10 cm. Results are shown for the support materials of anterior mockup_{ant} (support_{ant}) and posterior mockup_{pos} (support_{pos}), and attenuation fractions directly under the conductors. If applicable, the attenuation of a single wire and a double wire (crossing point) are both reported.

Prototype	Attenuation (A_{EPID})
Support _{ant} only	$-0.2\% \pm 0.1\%$
Support _{pos} only	$-0.4\% \pm 0.1\%$
Support _{ant} + wire _{1.8} (single/double)	$-1.4\% \pm 0.1\% / 2.8\%$
Support _{ant} + wire _{1.1} (single/double)	$-0.8\% \pm 0.1\% / 1.4\%$
Support _{ant} + wire _{1.0} (single/double)	$-0.8\% \pm 0.2\% / 1.3\%$

Table 3. Dose attenuation fractions that were found with simulations (A_{sim}) due to the anterior support materials and wire_{1.1} cable at 1.5 T. If applicable, the attenuation of a single cable and a double cable (crossing point) are both reported. For some larger angles the dose profile at 100 mm fell outside of the scoring region.

Prototype	Angle ($^{\circ}$)	A_{sim} (13 mm)	A_{sim} (100 mm)
Support only*	0	$-0.1\% \pm 0.2\%$	$-0.2\% \pm 0.2\%$
	30	$-0.1\% \pm 0.2\%$	$-0.2\% \pm 0.2\%$
	-30	$-0.0\% \pm 0.2\%$	$-0.2\% \pm 0.3\%$
	55	$-0.3\% \pm 0.2\%$	Not visible
	-55	$-0.1\% \pm 0.2\%$	Not visible
Support + wire _{1.1} (single/double)	0	$-0.8\% \pm 0.1\% / -1.5\%$	$-0.8\% \pm 0.2\% / -1.3\%$
	30	$-1.0\% \pm 0.2\% / -1.4\%$	$-0.9\% \pm 0.2\%$
	-30	$-0.9\% \pm 0.2\% / -1.5\%$	$-1.0\% \pm 0.3\%$
	55	$-1.5\% \pm 0.2\% / -2.1\%$	Not visible
	-55	$-1.3\% \pm 0.2\% / -2.0\%$	Not visible

* Extracted from the conductor-free regions of the wire_{1.1} simulation.

3.2. Imaging

Figure 7 shows the SNR maps of the single-channel prototypes. Depth profiles are plotted and show that the SNR on the anterior side is similar for all three prototypes, although wire_{1.0} produces the highest SNR. From 7 cm onwards, the wire_{1.0} and wire_{1.1} profiles overlap. All profiles end up at a similar asymptotic SNR value of around 5.0.

Figure 8 shows the SNR maps of the multi-channel arrays. The transverse plane is positioned at the center of the array in craniocaudal direction. Depth profiles are plotted and clearly show that the SNR on the anterior side is increased when the prototype array is used. The SNR more than doubles at the surface and ends up at a similar asymptotic SNR value. Figure 9 shows the noise correlation matrices of the HIC prototype and full clinical array. No significant coupling effects can be observed in the prototype, while the clinical array does show channel coupling between channels 2 and 3.

Radiation experiments showed that the SNR, determined in an ROI directly under the loop, was not affected by irradiation with a $15 \times 15 \text{ cm}^2$ beam. Figure 10 shows that both the single-channel prototype as well as the clinical array do not demonstrate a drop in SNR when radiation is turned on. Visual inspection revealed no signal changes or artifacts in the reconstructed images.

4. Discussion

In this work, we introduce HICs as a suitable building block of radiolucent receive arrays for MRI-guided radiotherapy, as they lack tuning capacitors that can attenuate the treatment beam. The use of HICs has many advantages from an imaging perspective: HICs are flexible, inherently decoupled due to their limited current flow, easy to manufacture, and easily detunable over a broad frequency range. In addition, they allow for the use of non-rigid, low-density support materials to create radiolucent and light-weight arrays for increased patient comfort.

In this work, we showed the design and demonstrated the dosimetric feasibility of a flexible on-body receive array using HICs and showed the design's impact on the surface dose and dose at depth. Additionally, we investigated the imaging performance of single-channel prototypes.

Minimization of the bolus effect, and thus the surface dose of the patient, due to on-body placement was achieved by placing a 10 or 15 mm spacer between the HICs and the skin (figure 6). Here, a conservative 15 mm distance is used for the dosimetry at depth and imaging measurements. When this 15 mm foam layer is placed, the HIC's dose imprint was resolved and anterior surface dose increase was only 7% of D_{max} , which we deemed

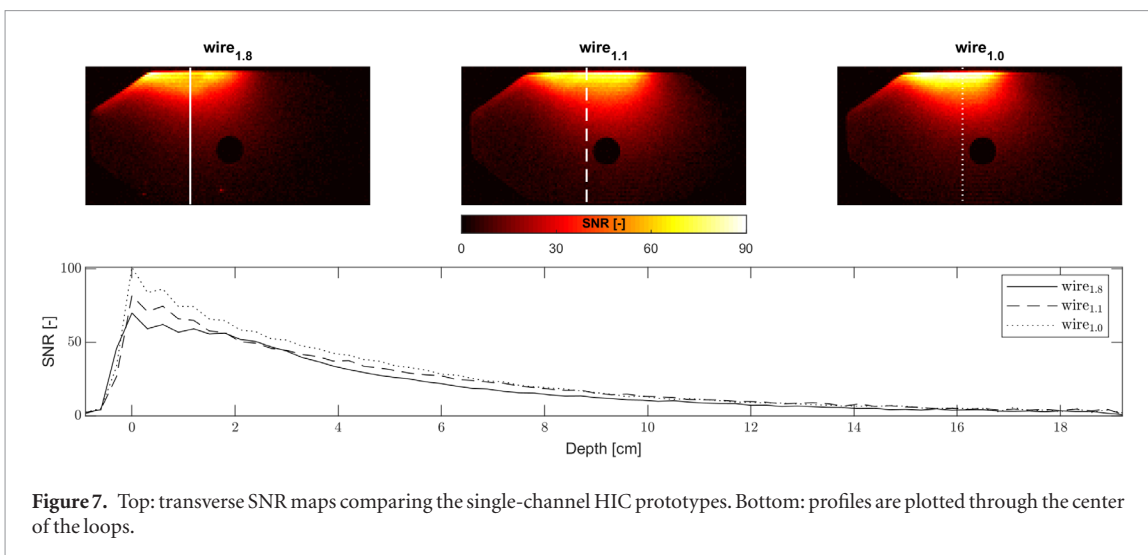


Figure 7. Top: transverse SNR maps comparing the single-channel HIC prototypes. Bottom: profiles are plotted through the center of the loops.

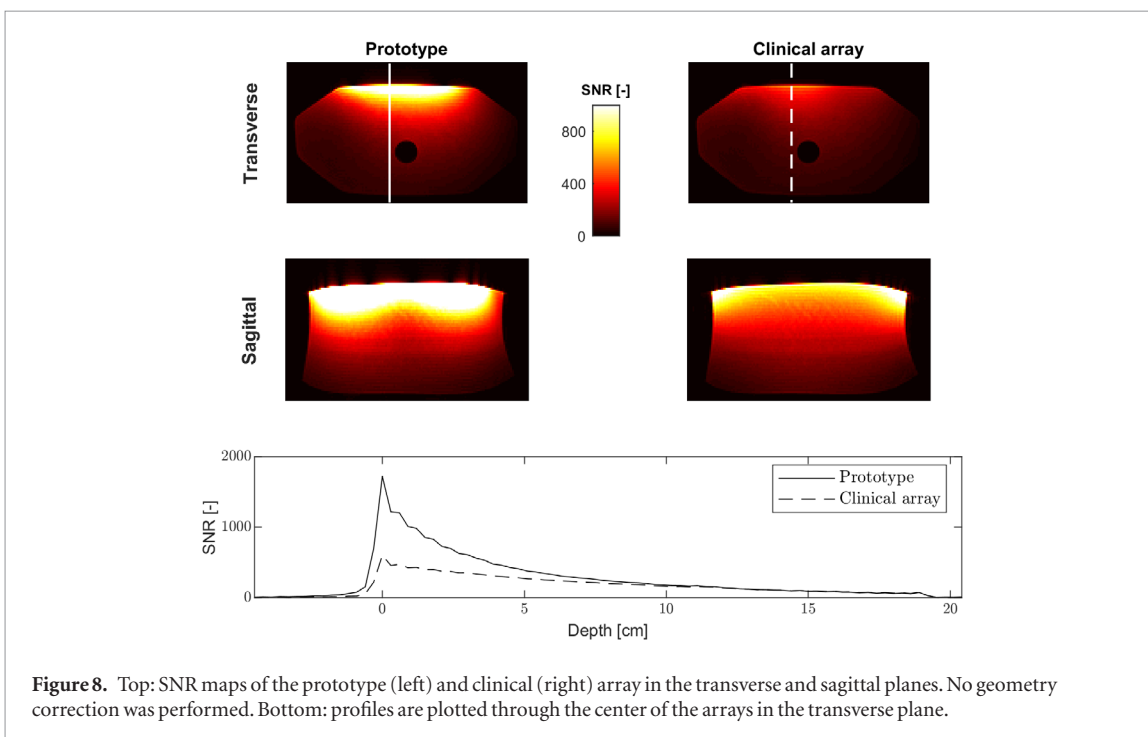


Figure 8. Top: SNR maps of the prototype (left) and clinical (right) array in the transverse and sagittal planes. No geometry correction was performed. Bottom: profiles are plotted through the center of the arrays in the transverse plane.

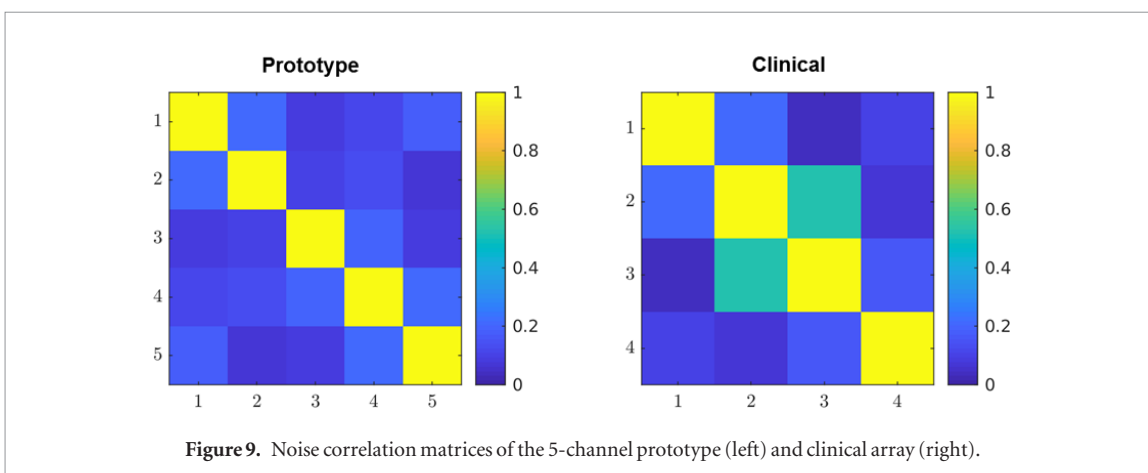
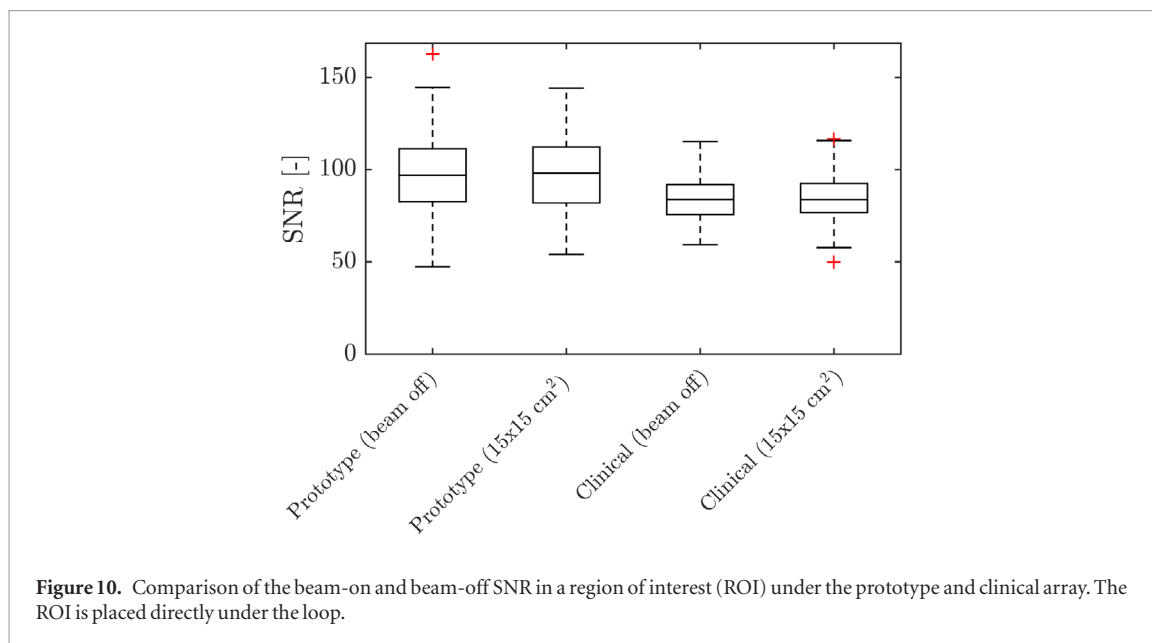


Figure 9. Noise correlation matrices of the 5-channel prototype (left) and clinical array (right).



acceptable. In comparison, the table currently increases the surface dose by 25% of D_{max} and is not considered problematic, as the introduction of high-energy beams and volumetric techniques have significantly decreased local surface doses. Moreover, direct placement of the posterior element under the patient may actually reduce the surface dose for posterior beams, as secondary electrons from the dense table may be curved away from the patient in the low-density support materials. On-body placement of the array does change the body outline and thus hinders the use of pre-calculated treatment plans that use a CT scan (without receive array) as reference image. However, current clinical practice for the MR-linac already includes adaptation of the treatment plan to the anatomy of the day (adapt-to-shape) and therefore no longer requires an intact body contour. On-body placement should therefore pose no problem for MRI-guided radiotherapy treatments.

Dosimetry at a depth of 10 cm showed that the prototypes with the two thinnest cables result in maximal local dose changes of $\leq 0.8\%$ under a single cable and $\leq 1.4\%$ under a crossing point. The use of wire_{1,8} induced higher dose changes: -1.4% and -2.8% under the single cable and crossing points, respectively. Monte Carlo simulations with and without the magnetic field resulted in similar findings and matched well with the EPID dosimetry. Angulated simulations showed that the local dose reductions at depth increased up to 2.1% at a depth of 13 mm. Interestingly, the negatively angulated simulations led to an increased surface dose, while a positive angle reduced the surface dose with respect to the 0° situation. This is partially due to secondary electrons from the support materials that are curved away from the phantom by the Lorentz force and thus deposit less dose at the surface. Secondary electrons from the phantom's surface will also be curved away from the phantom and may partially be absorbed by the support materials, thus reducing the surface dose.

The clinical impact of all conductor-induced dose changes is deemed negligible, as slight, local underdosages from one beam will be smeared out due to physiological motion and clinical multi-angle beam or volumetric arc treatments. Clinically, local dose changes are expected to stay below 1%, which needs to be verified with dosimetry of a full multi-angle treatment using a full 32-channel array. If this proves to be the case, the full array can be disregarded during treatment planning. Hence, the array will have little impact on the clinical MR-linac workflow.

We demonstrated that the wire_{1,0} imaging prototype performed best, shortly followed by wire_{1,1}. Wire_{1,1} was found to be more durable and was therefore used in the multi-channel array. The 5-channel prototype clearly outperformed the clinical array: SNR at the surface more than doubled and became similar at larger depths. Expansion of the array to 32 channels will further improve the SNR and, more importantly, the PI capabilities for accelerated imaging. The flexible nature of the array will allow for optimal imaging sensitivity by folding around the patient. Irradiation of the HIC while imaging did not pose any problems and did not influence the measured SNR.

This work focused on the dosimetric feasibility of a radiolucent on-body array for MRI-guided radiotherapy, but its low-attenuating design also makes it interesting for application in hybrid PET/MRI systems. In this diagnostic application, the photons that are generated in a patient need to pass through the array to reach the PET detector. However, the attenuation of 511 keV photons will be different and must be assessed. Furthermore, other sites may also benefit from the flexible properties of the design, for example in the head and neck.

Theoretically, a low-impedance coil conductor can be thinner and could therefore lower local dose changes directly under the conductors of the array. However, the use of LICs poses severe challenges that complicate the design of a radiolucent MRIGRT receive array with a high channel count. An increased number of channels will result in narrower LICs, which in turn increases channel coupling. This can be mitigated to a certain degree by coil overlapping. However, this is only partially effective and requires rigid support materials, which in turn reduce the design's radiolucency. Adding more tuning capacitors (i.e. segmentation) is also not possible due to their beam attenuation. Additionally, gamma radiation can change the effective capacitance and consequently the coil's resonance frequency (Hamman 1971, Ferreira and Souza 2017). This effect should be further investigated in future work. HICs do not require tuning capacitors, thereby avoiding this issue altogether. Furthermore, this work shows that the use of HICs is dosimetrically feasible and, as discussed before, the advantages of HICs for imaging are abundant.

Future work will aim at manufacturing a full 32-channel array using the design described in this work. Realistic treatment plans with beams from multiple angles can then be delivered to show the final dosimetric impact of the array. Furthermore, a quantitative analysis of the PI performance of this array will show the potential acquisition time reduction.

5. Conclusion

In conclusion, the design of a flexible, on-body receive array was presented and was shown to be suitable for MRI-guided radiotherapy. HICs were shown to allow for dense placement of channels in a flexible radiolucent array without the coupling issues that LICs would exhibit. Surface dose increases were kept to a minimum with low-density foam spacers. The dosimetric impact at depth, even directly under the conductors, is acceptably low and will be further reduced by anatomical motion and the use of multiple beam angles. Wire_{1,0} and wire_{1,1} outperform wire_{1,8}, both dosimetrically and in image quality. Beam-on imaging is possible and the radiation does not affect the SNR. Future research with a full array will have to show the gain in PI performance and thus acquisition time reduction.

Acknowledgments

This work is part of the research program HTSM with project number 15354, which is financed by the Netherlands Organization for Scientific Research (NWO). We thank André Wopereis for his help with the EPID measurements. We also extend thanks to David W O Rogers and the Carleton Laboratory for Radiotherapy Physics for granting the use of the Carleton Physics Department CPU computing cluster.

Appendix A. EPID dosimetry validation

The EPID signal response is expected to be linear with dose (Grein *et al* 2002). This was validated by comparing the EPID signal response to ionization chamber measurements.

A.1. Methods

EPID measurements and attenuation calculations (A_{EPID}) were performed as described in section 2.2.2. Ionization chamber measurements used a 0.6 cm³ NE2571 Farmer type ionization chamber (NE Technology Limited, Berkshire, England) in solid water at a depth of 10 cm and with a slightly lower SSD of 144 cm. The same 10 × 10 cm² field size was used but with a 0° gantry angle. The dose attenuation fractions were calculated with

$$A_{\text{ion chamber}} = \frac{Q_{\text{object}} - Q_{\text{open}}}{Q_{\text{open}}}, \quad (\text{A.1})$$

where Q_{object} and Q_{open} are the measured charges with and without an object on the phantom. Ionization chamber measurements were performed three times per setup.

A.2. Results

Table A1 shows that the dose attenuation fractions that are measured using an EPID and an ionization chamber are similar. The attenuation of 10 mm solid water and 1 mm copper are slightly under- and overestimated by the EPID, respectively. With an R^2 of 0.95 with respect to the identity line, the signal-dose linearity assumption is found to be reasonable.

Table A1. Dose attenuation fractions that were found with ionization chamber ($A_{ion\ chamber}$) and EPID (A_{EPID}) measurements. Values are shown for several objects that are placed against 100 mm solid water.

Object (+100 mm solid water)	$A_{ion\ chamber}$ (%)	A_{EPID} (%)
Support anterior element	-0.17 ± 0.04	-0.2 ± 0.2
2 mm solid water	-0.76 ± 0.04	-0.8 ± 0.2
5 mm solid water	-1.99 ± 0.00	-1.8 ± 0.2
10 mm solid water	-3.91 ± 0.00	-3.4 ± 0.2
1 mm copper	-2.59 ± 0.07	-2.9 ± 0.2

Table B1. Comparison of the dose attenuation fractions at a depth of 10 cm that are measured with EPID dosimetry (A_{EPID}) and Monte Carlo simulations (A_{sim}) at 0 T and 1.5 T. If applicable, the attenuation of a single cable and a double cable (crossing point) are both reported.

Prototype	A_{EPID} (0 T)	A_{sim} (0 T)	A_{sim} (1.5 T)
Support only	$-0.2\% \pm 0.1\%$	$-0.2\% \pm 0.2\%$	$-0.2\% \pm 0.2\%$
Support + wire _{1,8} (single/double)	$-1.4\% \pm 0.1\% / -2.8\%$	$-1.7\% \pm 0.3\% / -3.0\%$	$-1.7\% \pm 0.2\% / -3.0\%$
Support + wire _{1,1} (single/double)	$-0.8\% \pm 0.1\% / -1.4\%$	$-0.8\% \pm 0.2\% / -1.3\%$	$-0.8\% \pm 0.2\% / -1.3\%$
Support + wire _{1,0} (single/double)	$-0.8\% \pm 0.2\% / -1.3\%$	Not available	$-0.7\% \pm 0.2\% / -1.1\%$

Appendix B. Impact of the magnetic field on the attenuation

The magnetic field is expected to have no influence on the dose at a depth of 10 cm. Here, the impact of the magnetic field is investigated.

B.1. Methods

The EPID dosimetry results were taken from table 2. The results of the simulations with a 1.5 T magnetic field were taken from table 3. These simulations were repeated without a magnetic field (0 T) to investigate the influence of the field strength on the dose.

B.2. Results

Table B1 shows the dose attenuation fractions that were found with the three methods. The simulations show no impact of the magnetic field on the dose changes that were found. The EPID dosimetry matches well with the simulations, although the wire_{1,8} attenuation values are slightly lower than in the simulations.

ORCID iDs

Stefan E Zijlema  <https://orcid.org/0000-0001-6541-1239>

Rob H N Tijssen  <https://orcid.org/0000-0003-1355-7150>

Sara L Hackett  <https://orcid.org/0000-0002-4987-3991>

References

- Breuer F A, Blaimer M, Heidemann R M, Mueller M F, Griswold M A and Jakob P M 2005 Controlled aliasing in parallel imaging results in higher acceleration (CAIPIRINHA) for multi-slice imaging *Magn. Reson. Med.* **53** 684–91
- Burke B, Fallone B G and Rathee S 2010 Radiation induced currents in MRI RF coils: application to linac/MRI integration *Phys. Med. Biol.* **55** 735
- Fallone B G 2014 The rotating biplanar linac-magnetic resonance imaging system *Semin. Rad. Oncol.* **24** 200–2
- Ferreira E D S and Souza J S 2017 Gamma radiation in ceramic capacitors: a study for space missions *J. Phys.: Conf. Ser.* **911** 012004
- Ghila A, Fallone B G and Rathee S 2016 Influence of standard RF coil materials on surface and buildup dose from a 6 MV photon beam in magnetic field *Med. Phys.* **43** 5808–16
- Grein E E, Lee R and Luchka K 2002 An investigation of a new amorphous silicon electronic portal imaging device for transit dosimetry *Med. Phys.* **29** 2262–8
- Hamman D J H 1971 Radiation effects design handbook. Section 3—Electrical insulating materials and capacitors *Technical Report NASA*
- Hoogcarspel S J, Crijns S P M, Lagendijk J J W, van Vulpen M and Raaymakers B W 2013 The feasibility of using a conventional flexible RF coil for an online MR-guided radiotherapy treatment *Phys. Med. Biol.* **58** 1925–32
- Hoogcarspel S J, Zijlema S E, Tijssen R H N, Kerkmeijer L G W, Jürgenliemk-Schulz I M, Lagendijk J J W and Raaymakers B W 2018 Characterization of the first RF coil dedicated to 1.5 T MR guided radiotherapy *Phys. Med. Biol.* **63** 025014
- Kawrakow I and Rogers D W O 2000 The EGSnrc code system: Monte Carlo simulation of electron and photon transport *Technical Report National Research Council Canada, Ottawa, Canada*
- Keall P J, Barton M and Crozier S 2014 The Australian magnetic resonance imaging-linac program *Semin. Rad. Oncol.* **24** 203–6

- Kellman P and McVeigh E R 2005 Image reconstruction in SNR units: a general method for SNR measurement *Magn. Reson. Med.* **54** 1439–47
- Lagendijk J J W, Raaymakers B W and van Vulpen M 2014 The magnetic resonance imaging-linac system *Semin. Rad. Oncol.* **24** 207–9
- Larkman D J, Hajnal J V, Herlihy A H, Coutts G A, Young I R and Ehnholm G 2001 Use of multicoil arrays for separation of signal from multiple slices simultaneously excited *J. Magn. Reson. Imaging* **13** 313–7
- Malkov V N and Rogers D W O 2016 Charged particle transport in magnetic fields in EGSnrc *Med. Phys.* **43** 4447–58
- McDermott L N, Louwe R J W, Sonke J J, van Herk M B and Mijnheer B J 2004 Dose-response and ghosting effects of an amorphous silicon electronic portal imaging device *Med. Phys.* **31** 285–95
- Mutic S and Dempsey J F 2014 The ViewRay system: magnetic resonance-guided and controlled radiotherapy *Semin. Rad. Oncol.* **24** 196–9
- Pruessmann K P, Weiger M, Scheidegger M B and Boesiger P 1999 SENSE: sensitivity encoding for fast MRI *Magn. Reson. Med.* **42** 952–62
- Raaijmakers A J E, Raaymakers B W and Lagendijk J J W 2005 Integrating a MRI scanner with a 6 MV radiotherapy accelerator: dose increase at tissue-air interfaces in a lateral magnetic field due to returning electrons *Phys. Med. Biol.* **50** 1363–76
- Sijbers J, den Dekker A J, Van Audekerke J, Verhoye M and Van Dyck D 1998 Estimation of the noise in magnitude MR images *Magn. Res. Imaging* **16** 87–90
- Vaughan J T, Hetherington H P, Otu J O, Pan J W and Pohost G M 1994 High frequency volume coils for clinical NMR imaging and spectroscopy *Magn. Reson. Med.* **32** 206–18
- Wulff J, Zink K and Kawrakow I 2008 Efficiency improvements for ion chamber calculations in high energy photon beams *Med. Phys.* **35** 1328–36
- Zhang B, Sodickson D K and Cloos M A 2018 A high-impedance detector-array glove for magnetic resonance imaging of the hand *Nat. Biomed. Eng.* **2** 570–7